Degradation diagnostics for lithium ion cells

Christoph R. Birkl [a], Matthew R. Roberts [b], Euan McTurk [b, c], Peter G. Bruce [b], David A. Howey [a, *]

[a] Department of Engineering Science, University of Oxford, OX1 3PJ, Oxford, UK
[b] Department of Materials, University of Oxford, OX1 3PH, Oxford, UK
[c] Warwick Manufacturing Group, University of Warwick, Warwick, CV4 7AL, UK

HIGHLIGHTS

- A diagnostic algorithm to identify and quantify degradation modes in Li-ion cells.
- Experimental proof for effects of degradation modes on the open circuit voltage.
- State of health estimations for commercial cells by fitting open circuit voltages.

GRAPHICAL ABSTRACT
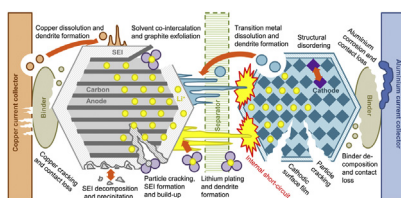
ABSTRACT

Degradation in lithium ion (Li-ion) battery cells is the result of a complex interplay of a host of different physical and chemical mechanisms. The measurable, physical effects of these degradation mechanisms on the cell can be summarised in terms of three degradation modes, namely loss of lithium inventory, loss of active positive electrode material and loss of active negative electrode material. The different degradation modes are assumed to have unique and measurable effects on the open circuit voltage (OCV) of Li-ion cells and electrodes. The presumptive nature and extent of these effects has so far been based on logical arguments rather than experimental proof. This work presents, for the first time, experimental evidence supporting the widely reported degradation modes by means of tests conducted on coin cells, engineered to include different, known amounts of lithium inventory and active electrode material. Moreover, the general theory behind the effects of degradation modes on the OCV of cells and electrodes is refined and a diagnostic algorithm is devised, which allows the identification and quantification of the nature and extent of each degradation mode in Li-ion cells at any point in their service lives, by fitting the cells' OCV.

© 2016 The Authors. Published by Elsevier B.V. This is an open access article under the CC BY license (http://creativecommons.org/licenses/by/4.0/).

1. Introduction

Lithium ion (Li-ion) cells degrade as a result of their usage and exposure to environmental conditions [1–4]. This degradation affects the cells' ability to store energy, meet power demands and, ultimately, leads to their end of life. Any system employing Li-ion cells as its power source must be informed of the amount of energy that can be stored and the power that can be provided by the battery at any point in time. Since the rates of capacity and power fade cannot be easily inferred from operational data in a practical system, methods and models are required which utilise available parameters and measurements to generate estimates and predictions of current and future energy storage capacity and power capability.

* Corresponding author.
E-mail addresses: christoph.birkl@eng.ox.ac.uk (C.R. Birkl), matthew.roberts@materials.ox.ac.uk (M.R. Roberts), e.mcturk@warwick.ac.uk (E. McTurk), david.howey@eng.ox.ac.uk (D.A. Howey).
URL: http://epg.eng.ox.ac.uk/

Degradation in Li-ion cells is caused by a large number of physical and chemical mechanisms, which affect the different components of the cells: the electrodes, the electrolyte, the separator and the current collectors [5–10]. Fig. 1 illustrates some of the most commonly reported degradation mechanisms in Li-ion cells. The different causes, rates and inter-dependencies of these degradation mechanisms make them extremely challenging to model, which is why most physics-based models focus only on the most dominant mechanisms, such as the formation and growth of the solid electrolyte interphase (SEI) [11,12] or electronic contact loss through particle cracking [13,14].

Physics-based models generally capture degradation at the micro scale, i.e. on a particle or even molecular level [13–15]. However, evidence suggests that meso and macro scale features, such as inhomogeneities in the structure of the electrodes, have a significant effect on cell degradation as a whole [16,17]. Structural non-uniformity can lead to inhomogeneous distributions of current densities and degrees of lithiation inside the electrode material, which in turn causes inhomogeneous degradation of the electrode. Evidence of such inhomogeneities has also been observed in the course of a post-mortem analysis of commercial Kokam pouch cells (described in detail in Section 2.1), which are the subject of this work. After low current rate (C/25) capacity tests, five cells were opened in an argon filled glove box and their electrode sheets visually inspected. Each cell consists of 20 sheets of positive (PE) and negative (NE) electrodes. Some of the investigated cells were fully charged, i.e. their negative graphite electrodes fully lithiated. Lithiated graphite has a golden color as opposed to the black color of delithiated graphite. Fig. 2 illustrates the difference in lithiation of graphite electrode sheets extracted from the same, fully charged cell. Whereas most NE sheets appeared to be uniformly lithiated (Fig. 2 a)), one NE sheet was clearly non-uniformly lithiated, as shown in Fig. 2 b). The cell was charged according to the test procedure specified in Table 3, with 100% SoC at the end of test. The standard deviation between the capacities of the five investigated pouch cells was less than 0.2% and the cell with one non-uniformly lithiated graphite sheet actually exhibited the highest capacity. This illustrates that meso- and macro-scale inhomogeneities can not
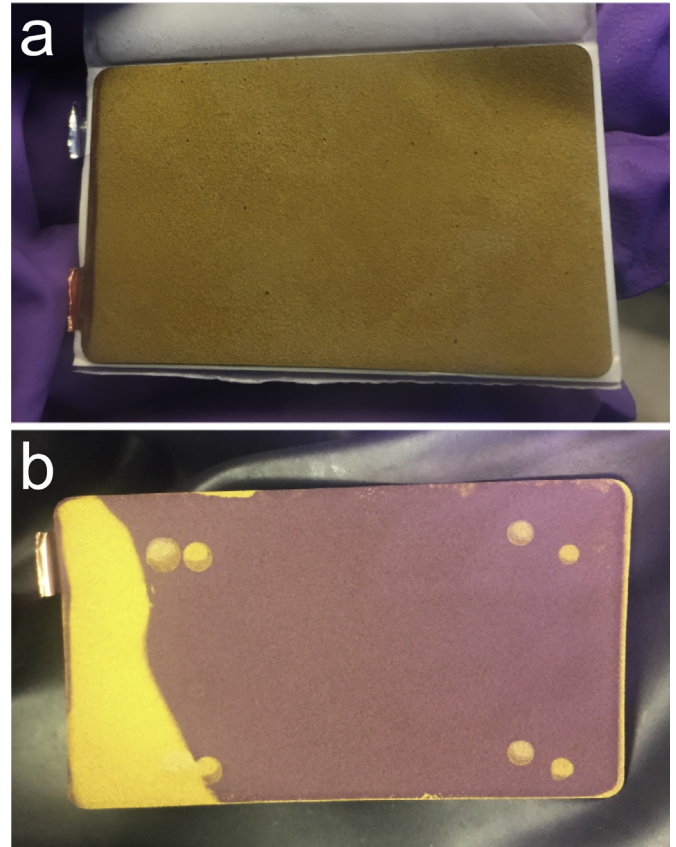
Fig. 2. Graphite negative electrodes extracted from a fully charged Kokam pouch cell; a) uniformly lithiated, b) non-uniformly lithiated.

easily be identified in commercial Li-ion cells but they may have long term effects on degradation. Bottom-up physics-based models may not be able to capture such inhomogeneities on a micro-scale.
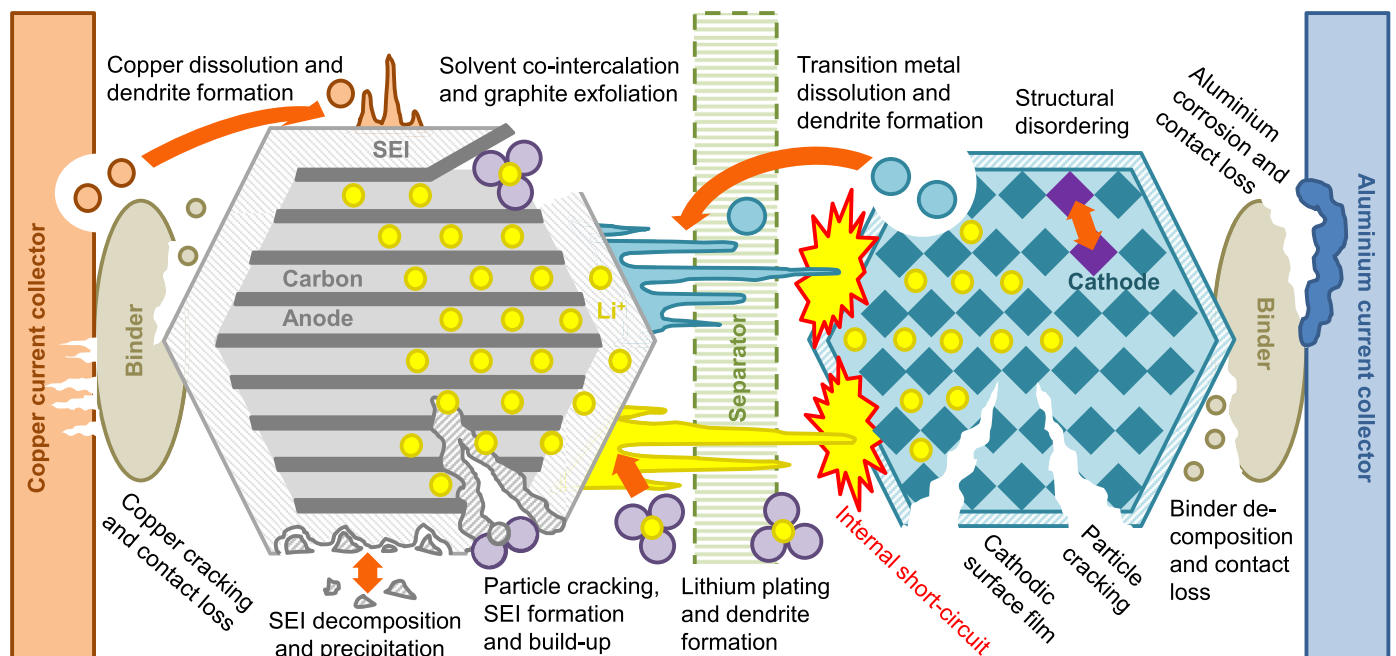
Fig. 1. Degradation mechanisms in Li-ion cells.

As an alternative, we propose to rely more heavily on a diagnostic approach, built on frequent cell characterisations using available measurements which include information on the state of health (SoH) of the cell. One such measurement is the cell's open circuit voltage (OCV). Since the OCV is the difference between the cathode and the anode voltage, it provides a thermodynamic fingerprint of the electrodes at any point in time. Changes in this fingerprint can offer valuable information on path-dependent degradation of both the individual electrodes and the cell as a whole. Not every degradation mechanism leaves a unique fingerprint in the cell's OCV but sets of mechanisms can be clustered into so-called degradation modes, which have a measurable effect on the OCV of the cell and the electrodes [18–21]. There are three commonly reported degradation modes:

1 **Loss of lithium inventory (LLI)**: lithium ions are consumed by parasitic reactions, such as surface film formation (e.g. SEI growth), decomposition reactions, lithium plating, etc. and are no longer available for cycling between the positive and negative electrode, leading to capacity fade. Surface films may also cause power fade. Lithium ions can also be lost if they are trapped inside electrically isolated particles of the active materials.
2 **Loss of active material of the NE (LAM$_{NE}$)**: active mass of the NE (or anode) is no longer available for the insertion of lithium due to particle cracking and loss of electrical contact or blocking of active sites by resistive surface layers. These processes can lead to both capacity and power fade.
3 **Loss of active material of the PE (LAM$_{PE}$)**: active mass of the PE (or cathode) is no longer available for the insertion of lithium due to structural disordering, particle cracking or loss of electrical contact. These processes can lead to both capacity and power fade.

A more comprehensive list of degradation mechanisms, their causes, effects and links to degradation modes is provided in Fig. 3. Note that Fig. 3 only lists the effects of degradation mechanisms and modes on the cell's thermodynamic (i.e. its OCV), not its kinetic behaviour. The primary effect of degradation on the cell's kinetics is an increase in internal resistance or cell impedance, which is easily measured by the voltage drop in response to a load. It should be noted that an increase in resistance can also lead to a decrease in useful cell capacity under load, since the lower voltage cut-off of the cell is reached sooner in a cell with a higher internal resistance. Equivalently, the higher voltage cut-off is reached sooner during charging. Methods to estimate internal cell resistance are widely reported [22–24] and not the subject of the presented work.

The assumed links between the OCV and degradation modes have been used for SoH estimation in the literature [19,25,26]. However, to the best of our knowledge, the existence of the proposed degradation modes has never been proven experimentally and unambiguously but only in simulation. Moreover, methods for estimating degradation modes and inferring the SoH of Li-ion cells are typically based on derivatives of OCV or cell capacity, so called incremental capacity analysis (ICA) [27] or differential voltage analysis (DVA) [28]. Differentiating measurements amplifies the noise in the signal and makes it more difficult to use the resulting data for processing. This is especially problematic in practical applications where voltage measurements may be noisier than in a laboratory environment. In response to these open questions and challenges, two primary objectives were defined for this work:

1. The design and execution of experiments to verify the manifestations of LLI, LAM$_{NE}$ and LAM$_{PE}$ on the OCV of Li-ion cells.
2. The creation of a diagnostic algorithm capable of identifying and quantifying the nature and extent of degradation modes present
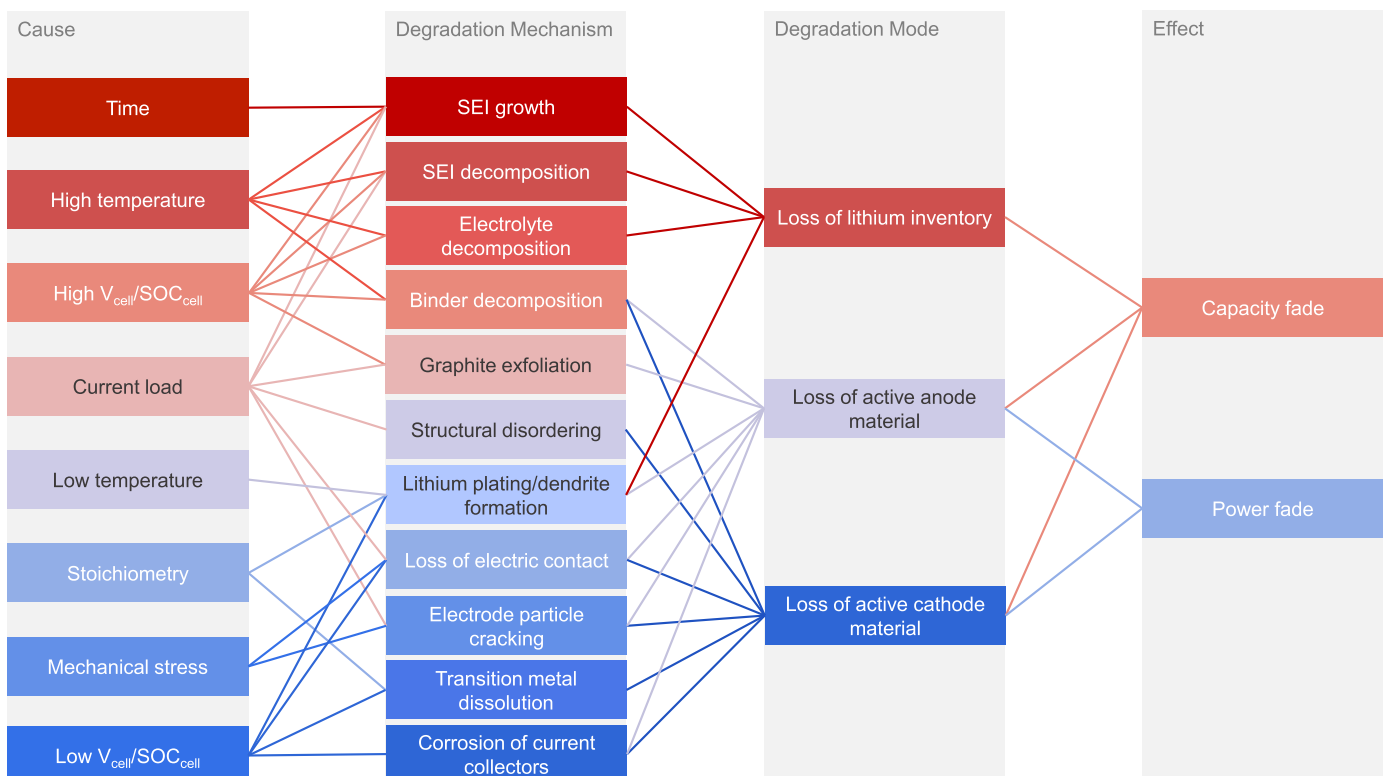

Fig. 3. Cause and effect of degradation mechanisms and associated degradation modes.

in a Li-ion cell based exclusively on the cell's OCV without performing derivative operations on the measurements.

2. Experimental

2.1. Material preparation

Coin cells were constructed with known amounts of lithium inventory and active electrode materials in order to emulate the different degradation modes. All coin cells were manufactured from electrodes harvested from commercial Kokam 740 mAh pouch cells. The NE material of the Kokam pouch cells is graphite and the PE material is a blend of lithium cobalt oxide (LCO) and lithium nickel cobalt oxide (NCO).

The pouch cells were opened in an argon filled glove box using a ceramic scalpel. The electrode sheets were extracted, rinsed with dimethyl carbonate and dried under vacuum for 20 min. The NE sheets consist of copper foil current collectors coated on both sides with graphite, and the PE sheets of aluminium foil current collectors coated on both sides with LCO/NCO. In order to improve electronic conductivity between the current collectors and the coin cell contacts, active material was removed from one side of the electrode sheets using N-methyl-2-pyrrolidone. The exposed Cu/Al surfaces were cleaned with dimethyl carbonate and the electrode disks were cut to size using hole punches. The coin cells were assembled using Celgard separators whetted with LP30 electrolyte (1.0 M LiPF$_6$ solution in ethylene carbonate (EC) and dimethyl carbonate (DMC); EC/DMC = 50/50).

Five reference cells were assembled with electrodes extracted from discharged (0% SoC) and fully charged (100% SoC) cells. Both positive and NE disks were cut to a diameter of 15 mm and the separator to 20 mm, as illustrated in Fig. 4 a). The reference cells served as a baseline against which the degradation modes were compared, and provided a measure for the reproducibility of the coin cell manufacturing process.

Two half-cells, one with positive and one with NE material, with 15 mm electrode disks were made in the same way as the full cells except with lithium foil as counter electrodes (see Table 1). The half-cells served to parametrize the OCV model, as described in Section 3.2. The reference cells and half-cells used in the experiments are listed in Table 1 along with the SoC of the electrodes at the time of assembly and the electrode disk diameters. The SoC of the electrodes refers to the degree of lithiation of the respective electrode at the time of assembly. For example, in a fully charged cell, the SoC of the PE is 0% and the SoC of the NE is 100%.

Loss of lithium inventory (LLI) was created by combining the PE of a pouch cell discharged to a higher SoC with the NE of a pouch cell discharged to a lower SoC. For example, combining a PE from a cell discharged to 25% SoC with a NE from a cell discharged to 0% creates a cell with 25% LLI, since the NE is the limiting electrode during discharge and once it has reached its upper voltage limit (the lower voltage limit of the cell), no more lithium can be extracted. In coin cells with emulated LLI, both electrode disks were 15 mm in diameter.

Loss of active electrode material was created by reducing the diameter of the respective electrode disk. The commercial electrodes extracted from the Kokam cells were very uniformly coated with active material, so the useful capacity of the electrodes was assumed to be proportional to their surface area. Loss of NE material (LAM$_{NE}$) was created by combining a larger PE disk with a smaller NE disk. Fig. 4 b) illustrates a cell with 36% LAM$_{NE}$, where the NE (anode) disk is 12 mm in diameter and the PE (cathode) disk is 15 mm in diameter. Loss of PE material (LAM$_{PE}$) was created by combining a larger NE disk with a smaller PE disk. Fig. 4 c) shows a cell with 36%
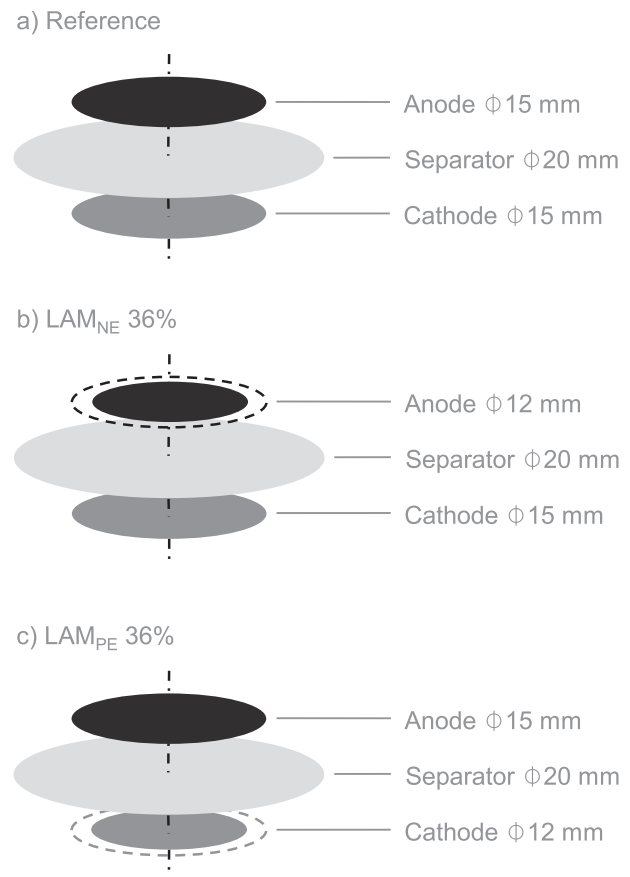

Fig. 4. Sizes of electrode disks and separators used in coin cells for a) reference cells and cells with LLI, b) cells with 36% LAM$_{NE}$ and c) cells with 36% LAM$_{PE}$.

LAM$_{PE}$, where the PE (cathode) disk is 12 mm in diameter and the NE (anode) disk is 15 mm in diameter. Theoretically, active electrode material can be lost in lithiated, delithiated and partially lithiated states. Loss of lithiated NE material (LAM$_{NE,li}$) was emulated by combining a 12 mm NE disk with a 15 mm PE disk, both harvested from a fully charged pouch cell (SoC = 100%). Equivalently, loss of delithiated NE material LAM$_{NE,de}$ was emulated by combining a 12 mm NE disk with a 15 mm PE disk, both harvested from a fully discharged pouch cell (SoC = 0%). The same principle was used to create loss of lithiated PE material (LAM$_{PE,li}$). A limitation of this experimental approach to simulate the loss of active material is the fact that lithium insertion/extraction in the overhang region of the larger electrode is limited by the lateral diffusion of lithium in the active material. The simulation of LAM using this method is therefore only valid for very slow C-rates. For this reason, a very low pseudo-OCV C-rate of C/25 is used in this work.

A combination of LLI and LAM$_{PE,li}$ was created by combining a 14 mm PE disk harvested from a pouch cell previously discharged

Table 1
Baseline cell and half-cell electrodes.

Reference cells	Coin cell ID	SoC PE	SoC NE	Diameter PE	Diameter NE
Full cells	Ref 1	100%	0%	15 mm	15 mm
	Ref 2	100%	0%	15 mm	15 mm
	Ref 3	100%	0%	15 mm	15 mm
	Ref 4	0%	100%	15 mm	15 mm
	Ref 5	0%	100%	15 mm	15 mm
Half-cells	HC$_{PE}$	100%	–	15 mm	–
	HC$_{NE}$	–	0%	–	15 mm

Table 2
Test cell electrodes.

Deg. mode	Coin cell ID	SoC PE	SoC NE	Diameter PE	Diameter NE
25% LLI	LLI25	75%	0%	20 mm	20 mm
50% LLI	LLI50	50%	0%	20 mm	20 mm
36% LAM$_{NE,li}$	LAM$_{NE,li}$	0%	100%	15 mm	12 mm
36% LAM$_{NE,de}$	LAM$_{NE,de}$	100%	0%	15 mm	12 mm
36% LAM$_{PE,li}$	LAM$_{PE,li}$	100%	0%	12 mm	15 mm
25% LLI+13% LAM$_{PE,li}$	LLI + LAM$_{PE}$	75%	0%	14 mm	15 mm

Table 3
Test procedure for pouch cell preparation.

SoC at end of test	Test step	Current	limits
0%	CC charge	29.6 mA	$V_{Cell} > 4.2V$
	CC discharge	29.6 mA	$V_{Cell} < 2.7V$
100%	CC charge	29.6 mA	$V_{Cell} > 4.2V$
	CC discharge	29.6 mA	$V_{Cell} < 2.7V$
	CC charge	29.6 mA	$V_{Cell} > 4.2V$
50%	CC charge	29.6 mA	$V_{Cell} > 4.2V$
	CC discharge	29.6 mA	$V_{Cell} < 2.7V$
	CC charge	29.6 mA	$V_{Cell} > 4.2V$
	Rest	0 mA	time > 10min
	CC discharge	29.6 mA	$Q_{dch} > 0.5 \times Q_{meas}$
25%	CC charge	29.6 mA	$V_{Cell} > 4.2V$
	CC discharge	29.6 mA	$V_{Cell} < 2.7V$
	CC charge	29.6 mA	$V_{Cell} > 4.2V$
	Rest	0 mA	time > 10min
	CC discharge	29.6 mA	$Q_{dch} > 0.75 \times Q_{meas}$

Table 4
Test procedure for coin cells.

	Test ID	Test step	Current	Limits
Full cells	Part. charge	CC charge	1.118 mA	$V_{Cell} > 4.2V$
	C/2 cycle	CC discharge	1.118 mA	$V_{Cell} < 2.7V$
		CC charge	1.118 mA	$V_{Cell} > 4.2V$
	Part. discharge	CC discharge	1.118 mA	$V_{Cell} < 3.75V$
	Part. charge	CC charge	0.089 mA	$V_{Cell} > 4.2V$
	C/25 cycle	CC discharge	0.089 mA	$V_{Cell} < 2.7V$
		CC charge	0.089 mA	$V_{Cell} > 4.2V$
PE half-cell	Part. charge	CC charge	1.118 mA	$V_{Cell} > 4.5V$
	C/2 cycle	CC discharge	1.118 mA	$V_{Cell} < 3.5V$
		CC charge	1.118 mA	$V_{Cell} > 4.5V$
	Part. discharge	CC discharge	1.118 mA	$V_{Cell} < 4.0V$
	Part. charge	CC charge	0.089 mA	$V_{Cell} > 4.5V$
	C/25 cycle	CC discharge	0.089 mA	$V_{Cell} < 3.5V$
		CC charge	0.089 mA	$V_{Cell} > 4.5V$
NE half-cell	Part. discharge	CC discharge	1.118 mA	$V_{Cell} < 0.001V$
	C/2 cycle	CC charge	1.118 mA	$V_{Cell} > 1.3V$
		CC discharge	1.118 mA	$V_{Cell} < 0.001V$
	Part. charge	CC charge	1.118 mA	$V_{Cell} > 0.1V$
	Part. charge	CC charge	0.089 mA	$V_{Cell} > 1.3V$
	C/25 cycle	CC discharge	0.089 mA	$V_{Cell} < 0.001V$
		CC charge	0.089 mA	$V_{Cell} > 1.3V$

to 25% SoC with a 15 mm NE disk harvested from a pouch cell previously discharged to 0% SoC.

Table 2 provides a list of all the coin cells manufactured to emulate the different degradation modes, including the SoC of the electrodes and the diameter of the electrode disks.

2.2. Cell testing

All cell tests were conducted in thermal chambers at 30 °C using BioLogic potentiostats of type MPG-205 and SP-150. Before the start of tests, pouch cells and coin cells were stored in the thermal chambers for 3 h for thermal equilibration. The pouch cells from which the electrodes were extracted for the coin cell manufacturing were prepared according to the test schedule listed in Table 3. Firstly, the capacities of the pouch cells (Q_{meas}) were measured during a C/25 (29.6 mA) discharge following a C/25 charge. Secondly, following another C/25 charge, the SoC of the pouch cells was adjusted by a C/25 discharge to the levels required for the respective coin cells, based on the initial capacity measurements.

The reference coin cells (full cells and PE/NE half-cells) and the coin cells with induced degradation modes were tested according to the test schedule in Table 4, which consisted primarily of one cycle at C/2 and one cycle at C/25. Partial charges/discharges served to adjust the cells' SoC in preparation for the full cycles, as listed in Table 4. The C/2 cycle served to assess the general performance of the cells, based on which under-performing cells were discarded, and the C/25 cycle served as pseudo-OCV measurement.

At a current rate of C/25, the voltage drop in the coin cells was measured to be on the order of 9×10^{-4}mV, which was considered negligible and any voltage measurements recorded at a current rate of C/25 were treated as pseudo-OCV. These pseudo-OCV measurements were used in the degradation model to estimate the degradation modes. The expected capacities of the coin cells were calculated based on the active surface areas of the electrodes. The total electrode surface area of the pouch cells was 600 cm² and

their average capacity measured at C/25 was 759 mAh with a standard deviation of < 0.2%. Given a surface area of 1.767 cm² in all coin cells with electrode diameters of 1.5 cm, the expected nominal coin cell capacity is 2.236 mAh, which gives a C/25 current of 0.089 mA and a C/2 current of 1.118 mA. The standard deviation of the capacities of all five reference coin cells measured at a C/2 current rate was 5.4%, which served as the measure of uncertainty for the estimation of degradation modes.

3. Model development

3.1. Theory

The theory underlying the proposed degradation modes and their effects on the OCV of cells and electrodes is well documented in the literature [19,26,29]. This section explains the approach and the extensions of the presented work.

In Li-ion cells, the end of charge (EoC; 100% SoC) and the end of discharge (EoD; 0% SoC) are defined by a corresponding maximum and minimum cell voltage, in order to ensure safe operation. The lithium cycled within these limits constitutes the cell's useful capacity. During charge, the PE is limiting, since its rising voltage, resulting from delithiation, triggers the cell's EoC voltage limit (in this case 4.2 V). Analogously, the NE is limiting during discharge, triggering the EoD voltage limit (in this case 2.7 V).

Fig. 5 a) shows the base case of a pristine cell. The bars on the left symbolise the anode (NE, in red) and the cathode (PE, blue). The areas of the bars represent the electrode capacities, not to scale. The golden area represents the cyclable lithium, which corresponds to the cell capacity, in this case intercalated in the NE in a fully charged cell. In commercial Li-ion cells, there is generally an excess of NE
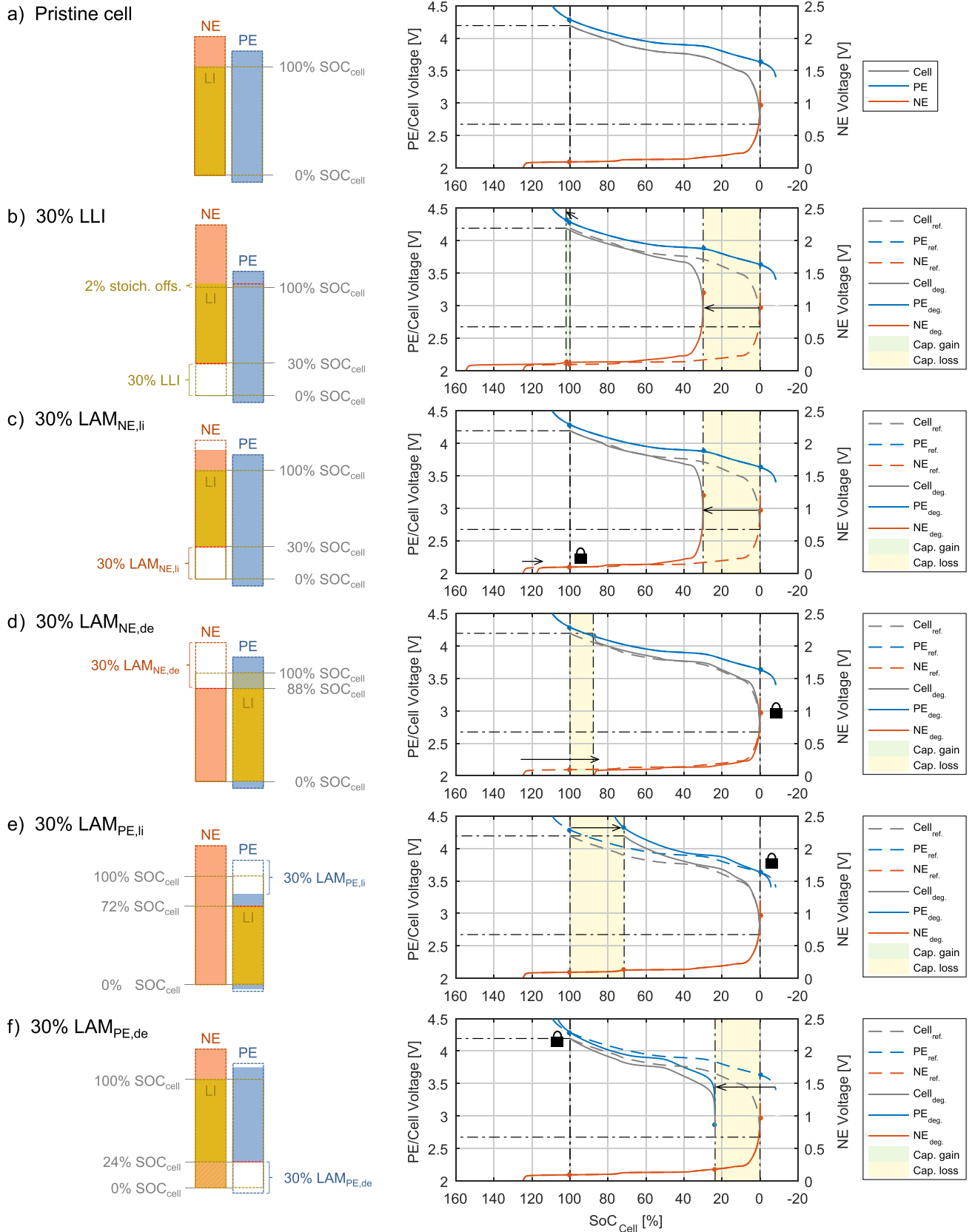
Fig. 5. Examples of the different degradation modes. The bars in the left column illustrate the utilisation of the electrodes as a result of the degradation modes, compared to the base case (not to scale). The plots on the right show the corresponding OCV of the electrodes and the cell.

material, which is illustrated by the larger NE bar. The misalignment of the two bars indicates which electrode is limiting at 100% SoC and 0% SoC, respectively. The plot on the right of Fig. 5 a) depicts the OCV curves of the PE in blue, the NE in red and the cell in grey, as functions of the cell's normalised capacity, denoted as SoC_{Cell} in %. The horizontal dash/dot lines highlight the upper and lower voltage limits of the cell at 4.2 V and 2.7 V, respectively, and the vertical dash/dot lines highlight the corresponding maximum and minimum SoC of the whole cell. The points on the OCV of the PE and NE that correspond to the cell's upper and lower voltage limits are indicated by circular markers on the respective OCV curves. As LLI, LAM_{NE} and LAM_{PE} come into effect, the utilised portions of the electrodes change, which is reflected in their OCVs. This means that the OCV of the electrodes at EoC and EoD may also change accordingly. The EoC and EoD OCVs of the electrodes are further affected by maintaining constant upper and lower cell voltage limits of 4.2 V and 2.7 V, respectively. Imposing these voltage limits can lead to a stoichiometric offset between the electrodes, which has not been addressed in the literature but is an important addition of this work. The effects of these offsets are discussed individually for each degradation mode.

If cyclable lithium is lost a smaller fraction of the electrodes' capacities is used, due to the increased offset between the positive and negative electrode. The example of 30% LLI is illustrated by both the shift of the bars on the left of Fig. 5 b) and the shift of the negative electrode's OCV curve in the plot on the right. The OCV curves of the base case are depicted for comparison as broken lines. The yellow areas in the plots on the right of Fig. 5 indicate lost cell capacity. The OCVs of the electrodes at the EoC and EoD are also affected by the stoichiometric offset due to the imposed cell voltage limits. When a cell which has lost 30% of its lithium inventory approaches its EoD (0% SoC), the PE voltage is significantly higher than it would be in a pristine cell at EoD (compare the two circular blue markers on the PE OCV curve at the EoD in Fig. 5 b)). If the cut-off voltage of the NE remained unchanged, the minimum cell voltage of 2.7 V could not be reached. In reality, as the cell approaches its EoD and the cell voltage is driven towards 2.7 V, more lithium is extracted from the NE and inserted into the positive electrode, leading to a steep rise in the NE voltage, ultimately reaching the minimum cell voltage of 2.7 V (compare the two circular red markers on the NE OCV curves at the EoD in Fig. 5 b)). Equivalently, as a cell with 30% LLI approaches its EoC, the NE voltage is higher than in a pristine cell. Therefore, as the cell is driven toward its upper voltage limit of 4.2 V, more lithium is extracted from the PE and inserted into the negative electrode, until the rise in PE voltage triggers the upper cut-off condition of the cell (compare the two circular blue markers on the PE voltage curve at the EoC in Fig. 5 b). In the case of 30% LLI, this stoichiometric offset causes a noticeable increase in cell capacity, on the order of 2%, as indicated by the green area in the OCV plot of Fig. 5 b). Driving the PE to ever higher voltages can destabilize the structure and, in the worst case, the delithiated cathode material reacts exothermically with the electrolyte, triggering thermal runaway [30].

The loss of lithiated active material in the NE ($LAM_{NE,li}$) can occur as a result of particle cracking or electronic contact loss between particles of the active electrode material or between the active material and the current collector. The lithium trapped inside the isolated graphite particles and can no longer be cycled, leading to a decrease in the cell's capacity. This capacity loss is illustrated by a shortened red/golden NE bar on the left of Fig. 5 c) and the yellow area in the OCV plot on the right of the figure. Less NE material remains to receive and release lithium, which is manifested in a shrinkage of the OCV curve of the NE, as shown in Fig. 5 c). Less NE material means that the current density on the remaining material is increased during cycling, which could in turn lead to accelerated

aging of the NE and, in the worst case, to lithium plating on the surface if the charging rates exceed the rates of lithium diffusion into graphite. In the event that only fully lithiated NE material is lost, the EoC voltage of the NE remains the same (as indicated by the padlock symbol in the plot of Fig. 5 c). The EoD voltage of the positive and negative electrodes change in the same manner as they would in the case of LLI (indicated by the circular markers).

The loss of delithiated NE material ($LAM_{NE,de}$) initially only has a small effect on the capacity of the cell, since there is an excess of NE material and the OCV of the NE at the EoD remains constant (see Fig. 5 d)). However, the OCV of the NE at the EoC gradually decreases as a result of the loss of active material, which limits the PE to a lower OCV at the EoC thus extracting less lithium. Once the remaining capacity of the NE is smaller than the original cell capacity, the cell loses capacity at the same rate as it loses active NE material. The capacity loss is equivalent to the portion of lithium inventory that remains trapped in the PE at higher voltages, which is indicated by the blue/gold striped area in the PE bar of Fig. 5 d). The example of 30% $LAM_{NE,de}$ illustrated in Fig. 5 d), effectively leads to a capacity loss of 12%. Moreover, since the cell is still driven to its upper voltage limit of 4.2 V, the NE can be forced to negative voltages, which initiates lithium plating. This is a mechanism that must be prevented in practical applications, since it can lead to dendrite formation and internal short-circuits, which in turn cause catastrophic cell failure [31,32].

The loss of lithiated PE material ($LAM_{PE,li}$) is analogous to $LAM_{NE,li}$; it is a result of electronic contact loss to lithiated PE particles. An example of 30% $LAM_{PE,li}$ is given in Fig. 5 e). The OCV curve of the PE shrinks compared to its original extent, since a smaller amount of active material contains less lithium and is discharged faster. At the cell's EoC, this means that less lithium is inserted into the NE, leaving it at a higher OCV, which must be matched by a higher OCV of the PE in order to reach the cell's upper voltage limit of 4.2 V. A similar scenario arises as discussed for the case of LLI - increasing $LAM_{PE,li}$ leads to ever higher PE voltages, potentially destabilizing the PE material.

A loss of delithiated PE material ($LAM_{PE,de}$) can potentially affect the cell capacity at early stages, since there is only a smaller buffer of PE material compared to that in the negative electrode. A scenario of 30% $LAM_{PE,de}$ is illustrated in Fig. 5 f). The OCV of both electrodes at the cell's EoC remains constant but the OCV of the PE at the cell's EoD decreases as the OCV curve of the PE shrinks compared to its original extent. In the case of commercial LCO/NCO material, there can be a steep drop in OCV below $\sim 3.4V$. Such a drop leads to an equivalently lower OCV of the NE at the cell's EoD (indicated by the circular markers in the OCV plot of Fig. 5 f)). The lithium inserted in the NE at higher NE voltages can no longer be accessed for cycling (illustrated by the red/gold striped pattern in the NE bar of Fig. 5 f)), which causes the observed capacity loss of 24%.

3.2. The OCV model

In previous work, we developed a parametric OCV model which can be used as a functional expression of the OCV of both the electrodes and the cell [33]. This OCV model is used as the basis for modelling and estimating the degradation modes discussed in this work. A brief account of the application of the OCV model is provided as follows. For a more detailed description, the reader is referred to [33].

The normalised capacity of an electrode can be expressed as the ratio x of occupied to available lattice sites in a host structure, ranging from 0 to 1. In solid multi-phase intercalation materials, x can be calculated as a function of the open circuit voltage E^{OC} by

$$x\left(E^{OC}\right) = \sum_{i=1}^{N} \frac{\Delta x_i}{1 + \exp^{(E^{OC} - E_{0,i})a_i e/kT}} \tag{1}$$

where N is the number of phases in the material, $i = \{1, 2, \ldots N\}$, Δx_i is the fraction of material attributed to phase i, $E_{0,i}$ is the energy of lattice sites in phase i, a_i is an approximation of the interaction energy between intercalated ions, e is the elementary charge, k is the Boltzmann constant and T the temperature in Kelvin.

In the first step of the OCV model parametrization, Equation (1) was fitted to the pseudo-OCV measurements of the PE and NE half-cells. In previous work, a minimum of four phases were identified in both the PE and NE material for this particular cell chemistry [33]. In this work, high qualities of fit of electrode OCVs are paramount in order to achieve accurate estimates of degradation modes. For this reason, an additional phase was added to the OCV model in order to improve the fit qualities from a root mean squared error (RMSE) of 7 mV for the PE and 12 mV for the NE [33] to < 3 mV for both electrodes in this work, as demonstrated in Fig. 6. Equation (1) can not be expressed explicitly as $E^{OC}(x)$ for multiple phases N and is therefore solved iteratively during the optimisation. The objective function used for the optimisation is

$$\arg_\theta \min \mathrm{RMSE} = \sqrt{\frac{\sum_i^n \left(\widehat{E}_i^{OC}(\theta) - E_i^{OC}\right)^2}{n}} \tag{2}$$

where n is the number of OCV measurements and $\widehat{E}_i^{OC}$ is the fitted electrode OCV. θ are the model parameters obtained for each electrode, summarised by

$$\theta = \begin{bmatrix} E_{0,1} & \Delta x_1 & a_1 \\ E_{0,2} & \Delta x_2 & a_2 \\ \vdots & \vdots & \vdots \\ E_{0,5} & \Delta x_5 & a_5 \end{bmatrix}. \tag{3}$$

In the second step of the OCV model parametrization, the OCVs of the electrodes were fitted simultaneously with the OCV of the cell - using pseudo-OCV measurements recorded on a full cell - using parameters θ of each electrode as an initial guess. The OCV of the cell was calculated by
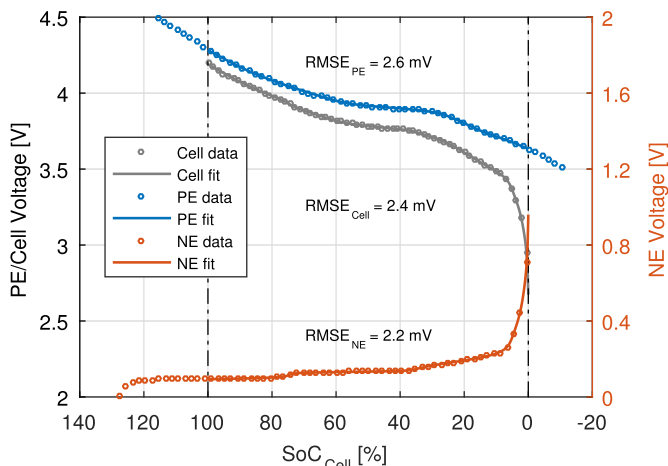
$$E_{Cell}^{OC} = E_{PE}^{OC} - E_{NE}^{OC}. \tag{4}$$

The objective function used for the second optimisation was

$$\arg_{\theta_{Cell}} \min \mathrm{RMSE} = \sqrt{\frac{\sum_i^n \left(\widehat{E}_{Cell,i}^{OC}(\theta_{Cell}) - E_{Cell,i}^{OC}\right)^2}{n}}$$
$$+ \sqrt{\frac{\sum_i^n \left(\widehat{E}_{PE,i}^{OC}(\theta_{Cell,PE}) - E_{PE,i}^{OC}\right)^2}{n}} \tag{5}$$
$$+ \sqrt{\frac{\sum_i^n \left(\widehat{E}_{NE,i}^{OC}(\theta_{Cell,NE}) - E_{NE,i}^{OC}\right)^2}{n}}.$$

Parameters θ_{Cell} can be summarised by

$$\theta_{Cell} = \begin{bmatrix} E_{0,PE,1} & \Delta x_{PE,1} & a_{PE,1} & E_{0,NE,1} & \Delta x_{NE,1} & a_{NE,1} \\ E_{0,PE,2} & \Delta x_{PE,2} & a_{PE,2} & E_{0,NE,2} & \Delta x_{NE,2} & a_{NE,2} \\ \vdots & \vdots & \vdots & \vdots & \vdots & \vdots \\ E_{0,PE,5} & \Delta x_{PE,5} & a_{PE,5} & E_{0,NE,5} & \Delta x_{NE,5} & a_{NE,5} \end{bmatrix}. \tag{6}$$

$\theta_{Cell,PE}$ and $\theta_{Cell,NE}$ in Equation (5) include the electrode parameters as detailed in Equation (3). Using the parameters θ_{Cell}, Equations (1) and (4) are applied in the degradation model to compute the OCVs and normalised capacities of electrodes and cells for the base case, i.e. a pristine cell without any signs of degradation. It is important to emphasize that the OCV model is only parameterized in this fashion once for the base case. Fitting the OCV of degraded cells, thus identifying the degradation modes, is achieved using the degradation model described below. This is based on the assumption that the degradation does not impact the individual phases of the electrode materials in different ways.

3.3. The degradation model

The degradation model is designed to estimate three parameters only; the degradation modes LLI, $\mathrm{LAM_{NE}}$ and $\mathrm{LAM_{PE}}$. The objective of the model is to estimate the extent of the different degradation modes at any point in a cell's life by fitting the cell's OCV. Only the full cell's OCV measurement is required for this. The parameters of the OCV model described in Section 3.2 remain unaltered.

The degradation modes affect the electrodes' capacity ranges in terms of (i) their offset, increased by LLI, (ii) their scaling, affected by $\mathrm{LAM_{NE}}$ and $\mathrm{LAM_{PE}}$ and (iii) the stoichiometric offset, at EoC (Δx_{EoC}) and EoD (Δx_{EoD}) due to the constant upper and lower cell voltage limits.

Equations (7)–(10) describe how LLI, $\mathrm{LAM_{PE}}$, $\mathrm{LAM_{NE}}$, Δx_{EoC} and Δx_{EoD} affect the normalised capacity of the PE at the cell's EoC ($x_{PE,EoC}$) and EoD ($x_{PE,EoD}$) and the normalised capacity of the NE at the cell's EoC ($x_{NE,EoC}$) and EoD ($x_{NE,EoD}$).

$$x_{PE,EoC} = \frac{\Delta x_{EoC}}{1 - \mathrm{LAM_{PE}}} \tag{7}$$

$$x_{PE,EoD} = \frac{\Delta x_{EoD} + 1 - \mathrm{LLI} + \mathrm{LAM_{PE}}}{1 - \mathrm{LAM_{PE}}} \tag{8}$$

$$x_{NE,EoC} = \frac{\Delta x_{EoC} + \mathrm{LLI} - \mathrm{LAM_{NE}}}{1 - \mathrm{LAM_{NE}}} \tag{9}$$

Fig. 6. OCV model fitting results.

$$x_{NE,EoD} = \frac{\Delta x_{EoD}}{1 - \text{LAM}_{NE}} \tag{10}$$

LLI, LAM_{PE} and LAM_{NE} in Equations (7)–(10) range from 0 to 1, where 1 is equivalent to the cell's original capacity; e.g. LLI = 0.1 means that the loss of lithium inventory is equivalent to 10% of the cell's original capacity. LAM_{PE} and LAM_{NE} refer to the loss of active material as a fraction of the active material originally utilised within the capacity range of the full cell. The normalised capacities of the positive and negative electrodes at EoC and EoD are linked through the cell's upper and lower voltage limits, denoted as $E^{OC}_{Cell,high}$ and $E^{OC}_{Cell,low}$, respectively, according to

$$E^{OC}_{Cell,high} - \widehat{E}^{OC}_{PE,EoC}(x_{PE,EoC}) + \widehat{E}^{OC}_{NE,EoC}(x_{NE,EoC}) = 0 \tag{11}$$

and

$$E^{OC}_{Cell,low} - \widehat{E}^{OC}_{PE,EoD}(x_{PE,EoD}) + \widehat{E}^{OC}_{NE,EoD}(x_{NE,EoD}) = 0. \tag{12}$$

Equations (11) and (12) define the OCV of electrodes and cell at 100% SoC and 0% SoC, respectively, when upper and lower cell voltage limits are imposed. The respective points on the OCV curves of cell and electrodes are marked by the vertical, dash/dotted lines in Fig. 5. $E^{OC}_{Cell,high}$ and $E^{OC}_{Cell,low}$ have predefined values, in this case 4.2 V and 2.7 V, respectively. $\widehat{E}^{OC}_{PE/NE,EoC}$ and $\widehat{E}^{OC}_{PE/NE,EoD}$ are the modelled OCV of the PE and NE at the EoC and EoD, respectively. The OCVs of the electrodes at the cell's EoC and EoD in Equations (11) and (12) ($\widehat{E}^{OC}_{PE,EoC}, \widehat{E}^{OC}_{NE,EoC}, \widehat{E}^{OC}_{PE,EoD}, E^{OC}_{NE,EoD}$) are calculated using Equation (1). Δx_{EoC} and Δx_{EoD} can be calculated by substituting Equations (7)–(10) into Equations (11) and (12) and solving the linear system of equations. The estimated LLI, LAM_{PE} and LAM_{NE} are inserted into Equations (7)–(10) during the optimisation described below.

The normalised capacity ranges of the electrodes in a degraded cell are defined by vectors of discrete values limited by the normalised capacities at the EoC and EoD according to Equations (13) and (14). The number of elements in the vectors depends on the number of sampling points obtained for the pseudo-OCV measurements.

$$\widehat{\mathbf{x}}_{\mathbf{PE}} = \{x_{PE,EoC}, \dots x_{PE,EoD}\} \tag{13}$$

$$\widehat{\mathbf{x}}_{\mathbf{NE}} = \{x_{NE,EoC}, \dots x_{NE,EoD}\} \tag{14}$$

The OCVs of the electrodes in a degraded cell ($\widehat{E}^{OC}_{PE}, \widehat{E}^{OC}_{NE}$) can thus be calculated by numerically solving Equation (1) for E^{OC} of the respective electrode, using the normalised electrode capacity ranges $\widehat{\mathbf{x}}_{\mathbf{PE}}$ and $\widehat{\mathbf{x}}_{\mathbf{NE}}$.

At the cell level, the normalised cell capacity at EoC and EoD is calculated using Equations (15) and (16).

$$x_{Cell,EoC} = \Delta x_{EoC} \tag{15}$$

$$x_{Cell,EoD} = 1 - \text{LLI} + \Delta x_{EoD} \tag{16}$$

In a pristine cell 100% SoC is equivalent to $x_{Cell,EoC} = 0$ and 0% SoC to $x_{Cell,EoD} = 1$. The cell's original capacity is normalised, so that $x_{Cell,EoD} - x_{Cell,EoC} = 1$. The difference between $x_{Cell,EoD}$ and $x_{Cell,EoC}$ in a degraded cell corresponds to the cell's normalised capacity as a fraction of its original capacity, e.g. $x_{Cell,EoD} - x_{Cell,EoC} = 0.9$ means that the cell has lost 10% of its original capacity. The normalised capacity range of the cell is defined by a vector of discrete values limited by $x_{Cell,EoC}$ and $x_{Cell,EoD}$ according to

$$\widehat{\mathbf{x}}_{\mathbf{Cell}} = \{x_{Cell,EoC}, \dots x_{Cell,EoD}\}. \tag{17}$$

Finally, the OCV of the degraded cell, $\widehat{E}^{OC}_{Cell,deg}$, is calculated for capacity range $\widehat{\mathbf{x}}_{\mathbf{Cell}}$, by solving Equation (2) using $\widehat{E}^{OC}_{PE}$ and $\widehat{E}^{OC}_{NE}$. Parameters LLI, LAM_{NE} and LAM_{PE} are estimated by minimising the objective function

$$\arg_{\theta_{deg}} \min \text{RMSE} = \sqrt{\frac{\sum_i^n \left(\widehat{E}^{OC}_{Cell,deg}(\theta_{deg}) - E^{OC}_{Cell,deg} \right)^2}{n}} \tag{18}$$

where $\widehat{E}^{OC}_{Cell,deg}$ is the calculated OCV of the degraded cell, $E^{OC}_{Cell,deg}$ is the measured pseudo-OCV of the degraded cell, n is the number of measurements and θ_{deg} are the parameters

$$\theta_{deg} = [\text{LLI, LAM}_{PE}, \text{LAM}_{NE}]. \tag{19}$$

The fitting procedure is carried out in Matlab, using the active-set algorithm in Matlab's *fmincon* optimisation function. In order to ensure convergence to the global minimum, the optimisation is run repeatedly (100 times) from different starting points using Matlab's global optimisation function *multistart*.

Since the cell's OCV drops off rapidly near the EoD, errors calculated at low OCV are generally greater than errors at higher OCV where the OCV curve is flat. In order to avoid a bias of the fit toward the lower end of the OCV curve, the calculation of the RMSE as described in Equation (18) was confined to the part of the OCV curve with a gradient of $\frac{\Delta E^{OC}_{Cell,deg}}{\Delta \text{SoC}} < 0.1$.

4. Results and discussion

4.1. OCV model fitting

The OCV model described in Section 3.2 and [33] was fitted to the pseudo-OCV measurements recorded on the electrode half-cells and a reference coin cell in order to obtain the OCV model parameters. High qualities of fit were achieved for both the OCV of the electrodes and the cell with root mean squared errors (RMSE) < 3mV (see Fig. 6). The solid lines in Fig. 6 show the fitted OCV results of the cell and the electrodes over the SoC range of the pristine cell. The high fitting accuracy is essential for the degradation model since any deviation from the actual OCV makes it more difficult to identify degradation modes, which may only have very slight effects on the OCV of a degraded cell. The estimated OCV model parameters - $E_{0,i}, a_i$ and Δx_i - for each of the phases $i = \{1\dots5\}$ of the PE and the NE are listed in Table 5.

4.2. Test of the diagnostic algorithm using synthesized data

With the OCV model parameterized, the degradation model described in Section 3.3 was used in 'forward mode' to create a number of scenarios of cells with known amounts of LLI, LAM_{PE} and LAM_{NE}. The OCVs of the hypothetical degraded cells were

Table 5
Estimated OCV model parameters.

	PE			NE		
	$E_{0,PE,i}$ [V]	$a_{PE,i}$ [1]	$\Delta x_{PE,i}$ [1]	$E_{0,NE,i}$ [V]	$a_{NE,i}$ [1]	$\Delta x_{NE,i}$ [1]
P_1	5.038	1.753	0.021	0.226	−18.072	0.025
P_2	4.079	0.178	0.523	0.219	−0.165	0.112
P_3	3.936	0.681	0.124	0.173	−1.188	0.243
P_4	3.900	3.074	0.136	0.132	−14.773	0.254
P_5	3.688	0.470	0.178	0.094	−6.690	0.365

subsequently used to test the ability of the diagnostic algorithm to identify the different degradation modes. It is important to point out that the model estimates the total amounts of lost active materials LAM_{PE} and LAM_{NE}, both lithitated and delithiated. Any lithium contained in lost active electrode material is included in the estimate of the total LLI; i.e. the total estimated LLI includes both the lithium lost through pure LLI (e.g. by SEI build up) and the lithium lost in lithiated active material ($LAM_{PE,li}$ and $LAM_{NE,li}$). For example, 10% of pure LLI and 5% of $LAM_{NE,li}$ gives a total of 15% LLI. The reason for the diagnostic algorithm to be designed in this manner is that a combination of e.g. LLI and $LAM_{NE,de}$ creates the same OCV signature as an equal amount of $LAM_{NE,li}$. The same holds true for combinations of LLI and LAM_{PE}. The fractions of lithiated and delithiated LAM can therefore not be uniquely identified if the assumption is that LLI can occur simultaneously, resulting from a different mechanism. An exceptional case would be one where LAM is detected but no LLI. In such a case, the respective LAM could be uniquely identified as loss of delithiated active material. In real-world scenarios of Li-ion cell degradation, there is no reason to assume that the loss of active electrode material occurs exclusively in lithiated or delithiated states - it is likely to occur over a range of different stages of lithiation. The approach to separate the loss of lithium contained in lost active electrode material from the loss of the active electrode material itself allows to account for these more realistic scenarios.

Three artificial scenarios were created to test the diagnostic algorithm by running the degradation model in 'forward mode'. The scenarios are listed in Table 6. The values in Table 6 are given as percentage of the cell's original capacity. Values of LAM refer to the loss of active material as a fraction of the active material originally utilised within the capacity range of the full cell.

The diagnostic algorithm was used to fit the degradation model to the synthetically generated cell OCVs, thereby identifying the amounts of total LLI, LAM_{PE} and LAM_{NE}. The fitting results are depicted in Fig. 7, which shows the fitted cell and electrode OCVs on the left (Fig. 7 a), c) and d)) and the amounts of real and estimated LLI, LAM_{PE} and LAM_{NE} on the right (Fig. 7 b), d) and f)). The dash/dotted horizontal lines in the OCV plots of Fig. 7 indicate the cell's upper and lower voltage limits and the vertical lines indicate the corresponding relative capacity. The broken lines show the OCVs of the electrodes and cell of the reference (pristine) cell. Areas filled with yellow indicate capacity loss. For all three scenarios, perfect fits were obtained and all degradation modes accurately identified, which proves the ability of the diagnostic algorithm to uniquely identify the three different degradation modes by fitting the OCV of a degraded cell.

4.3. Validation of the diagnostic algorithm using coin cell data

The diagnostic algorithm was used to estimate the degradation modes engineered by means of the customised coin cells (described in Section 2.1). The degradation model was fitted to the pseudo-OCV measurements recorded on the coin cells and the results are displayed in Fig. 8; OCV fitting results on the left and the extent of real and estimated degradation modes on the right. The broken lines in the OCV plots on the left of the figure show the cell and electrode OCV of the reference (pristine) cell. The filled areas at the EoC and EoD indicate capacity loss (in yellow) or capacity gain (in green) of the respective cell as a result of degradation. Capacity gain refers to the extraction of additional lithium from the PE as a result of the imposed upper cell voltage limit, leading to a stoichiometric offset. This can be detrimental to the cell, since the PE is driven to higher voltages, which may accelerate its degradation. The capacity gain at the EoC is never greater than the accompanying capacity loss at the EoD but it can slightly reduce the overall capacity loss. The RMSE values displayed in the OCV plots were calculated from the measured and the fitted cell voltages for the entire cell voltage window of 2.7 V–4.2 V. The error bars on the bar charts on the right of Fig. 8 are based on the standard deviation of the capacities of the reference coin cells (5.4%), as described in Section 2.2. It should be emphasized that the uncertainty of 5.4% reflects the reproducibility of the coin cell manufacturing. For applications on commercial cells, high accuracies can be expected for estimations of degradation modes, as demonstrated in Section 4.2. The results are discussed individually for each degradation scenario.

4.3.1. 25% LLI

The fitted OCV and estimated degradation mode of cell LLI25 (25% LLI) are shown in Fig. 8 a) and b), respectively. The diagnostic algorithm accurately estimated the extent of LLI within the margin of error (see Fig. 8 b)). The coin cell's OCV was fitted with a RMSE of 6.7 mV. The 25% LLI led to the expected increased offset between the positive and negative electrode's OCV, illustrated by a left-shift of the negative electrode's OCV in Fig. 8 a), which directly translates into capacity loss of the cell. The offset and imposed upper cell voltage limit forced the PE to a slightly higher OCV, extracting a small amount of additional lithium at the EoC, offsetting $\sim 1\%$ of the overall capacity loss. This is indicated by the dash/dotted vertical lines at the cell's EoC and the circular markers on the positive and negative electrode's OCV in Fig. 8 a).

4.3.2. 50% LLI

Fig. 8 c) and d) show the fitted OCV and estimated degradation mode of cell LLI50 (50% LLI). 50% LLI was accurately estimated and other degradation modes were found to be negligible within the margin of error. The RMSE of the OCV fit was 11.9 mV. The same trends were observed as for cell LLI25, albeit to a greater extent; a large offset between the positive and NE and a noticeably higher PE OCV at EoC, extracting an additional $\sim 2\%$ of lithium from the positive electrode. The results obtained for cells LLI25 and LLI50 confirm the theory of LLI discussed in Section 3.1.

4.3.3. 36% $LAM_{NE,li}$

Fig. 8 e) and f) show the fitted OCV and estimated degradation mode of cell $LAM_{NE,li}$ (36% $LAM_{NE,li}$). LAM_{NE} was successfully identified as a major degradation mode, although to a slightly smaller extent than expected, exceeding the margin of error by $\sim 4\%$. Against expectations, a small amount of LAM_{PE} was detected by the diagnostic algorithm, exceeding the margin of error by $\sim 5\%$. This discrepancy could be explained as an artifact of the coin cell manufacturing technique. The hole punch used to cut the 12 mm electrode disks slightly crimped the disks around the edge, causing a small rim which was bent away from the interface of electrode and separator. A rim of merely 0.3 mm around a 12 mm disk constains an additional 5% of the electrode's capacity. Due to the lack of contact between the rim around the NE disk (which was cut in a fully lithiated state) and the separator, the lithium contained in the NE could not be fully extracted during the pseudo-OCV discharge of the cell, which would appear as a loss of PE material. The fact that the extent of LAM_{NE} was underestimated by roughly the same amount as the LAM_{PE} was overestimated, namely between 4% and

Table 6
Scenarios for synthetic OCV data.

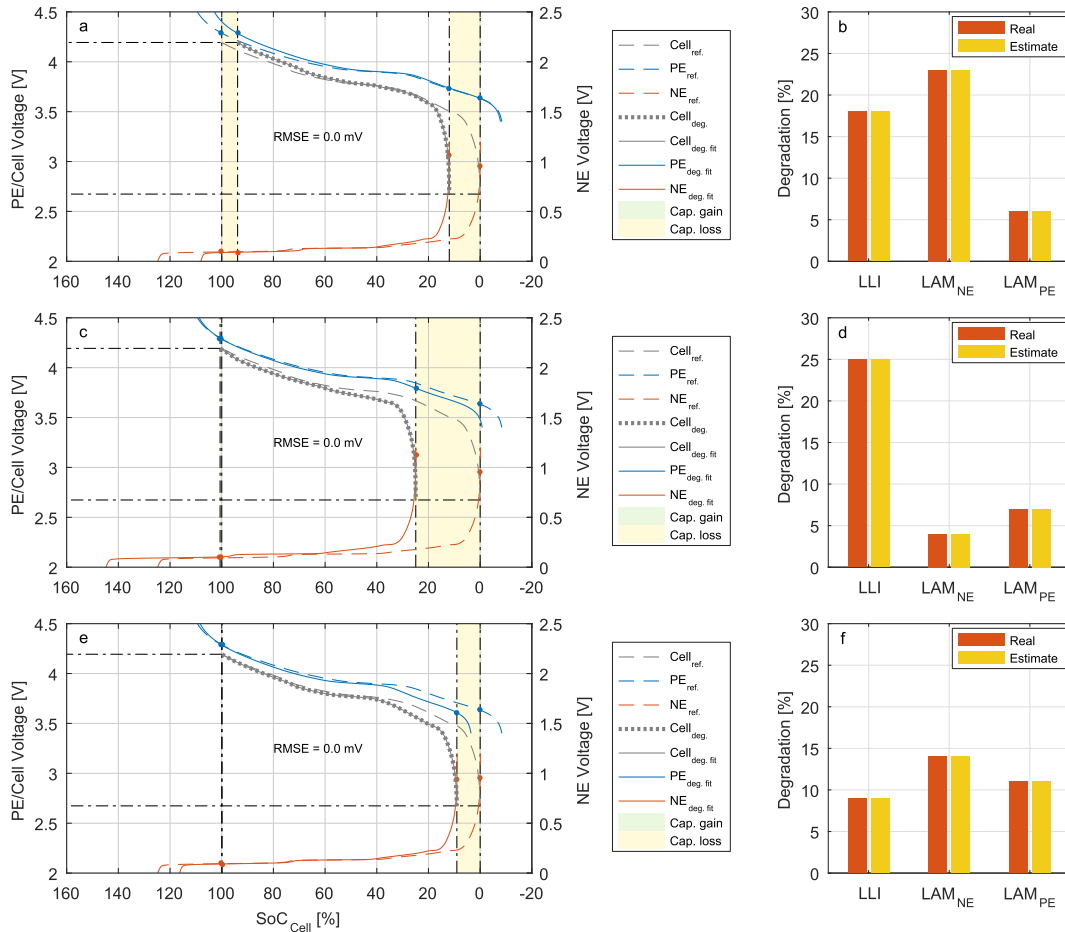| Scenario	LLI (pure)	$LAM_{NE,li}$	$LAM_{NE,de}$	$LAM_{PE,li}$	$LAM_{PE,de}$	LLI (total)
I	12%	0%	23%	6%	0%	18%
II	21%	4%	0%	0%	7%	25%
III	9%	0%	14%	0%	11%	9%

Fig. 7. Estimation of known amounts of LLI, LAM$_{PE}$ and LAM$_{NE}$; a) and b) Scenario I: 12% (pure) LLI, 23% LAM$_{NE,de}$, 6% LAM$_{PE,li}$, c) and d) Scenario II: 21% (pure) LLI, 4% LAM$_{NE,li}$, 7% LAM$_{PE,de}$, e) and f) Scenario III: 9% (pure) LLI, 14% LAM$_{NE,de}$, 11% LAM$_{PE,de}$.

5%, supports this theory. The lithium contained within the lost active NE material (LLI) was also slightly underestimated - to a similar degree as the LAM$_{NE}$, within the margin of error. Overall, the predominant degradation modes were correctly identified - LLI and LAM$_{NE}$. In this scenario, all of the lost lithium was contained in the lithiated negative electrode. The diagnostic algorithm correctly identified equal amounts of LLI and LAM$_{NE}$, suggesting that the prevalent mechanism was LAM$_{NE,li}$.

4.3.4. 36% LAM$_{NE,de}$

The diagnostic results for cell LAM$_{NE,de}$ are displayed in Fig. 8 g) and h) - fitted OCV and estimated degradation modes, respectively. Since a 36% loss of delithiated NE material exceeds the additional NE capacity buffer, lithium plating on the NE was expected in this scenario during charging. The onset of lithium plating occurs once the NE voltage drops below 0 V. The cells used in this work have a NE capacity buffer of ∼ 25%, which can be inferred from the OCV of the reference cell's negative electrode, shown as broken red line in the plots on the left of Fig. 8. The amount of LAM$_{NE,de}$ required to consume all of the NE buffer and reach the onset of lithium plating (LAM$_{NE,pl}$) can be calculated as follows. Firstly, the normalised capacity of the NE at $E_{NE}^{OC} = 0V$, scaled with respect to the normalised cell capacity ($x_{NE,Cell,pl}$), is calculated. $x_{NE,Cell,pl}$ is equivalent to the normalised and scaled capacity of the positive electrode, where $E_{PE}^{OC} = 4.2V$. The latter can be calculated using Equation (1) for the PE with 4.2 V plugged in as E_{PE}^{OC}, multiplying the result by the ratio of cell capacity to PE capacity and adding the offset between the

normalised cell capacity and the normalised PE capacity, which is equivalent to x_{PE} at $E_{Cell}^{OC} = 4.2V$ (as obtained by the OCV model). Now LAM$_{NE,pl}$ can be calculated using Equation (20).

$$LAM_{NE,pl} = 1 - \frac{x_{NE,cell,pl}}{x_{NE,Cell,max}} \tag{20}$$

where $x_{NE,max} = 1.25$ is the maximum of the normalised capacity of the negative electrode, scaled with respect to the cell capacity, in the reference cell. Equation (20) yields LAM$_{NE,pl} = 26.4\%$, which means that any loss of delithiated NE material exceeding 26.4% causes the onset of lithium plating on the NE and leads to further capacity loss due to irreversible deposition of metallic lithium. Although some of the lithium plated during charging may be recovered by stripping during discharging [34], the assumption in this work is that the amount of stripped lithium is negligible and any plated lithium leads to LLI. The amount of LLI resulting from plating can be approximated by calculating the difference between LAM$_{NE,de}$ and LAM$_{NE,pl}$, in this case amounting to 9.6% LLI. The diagnostic algorithm accurately identified both the amount of LAM$_{NE}$ and LLI within the margin of error, as shown in Fig. 8 h). The capacity loss attributed to LAM$_{NE,de}$ is illustrated by the yellow area at the cell's EoC in Fig. 8 g). Note that capacity lost due to lithium trapped inside the PE (yellow area in Fig. 8 g) at the cell's EoC), as a result of LAM$_{NE,de}$, is not included in the total amount of LLI. The capacity lost as a result of lithium plating is marked by the yellow area at the cell's EoD in Fig. 8 g). The small amount of LAM$_{PE}$ which
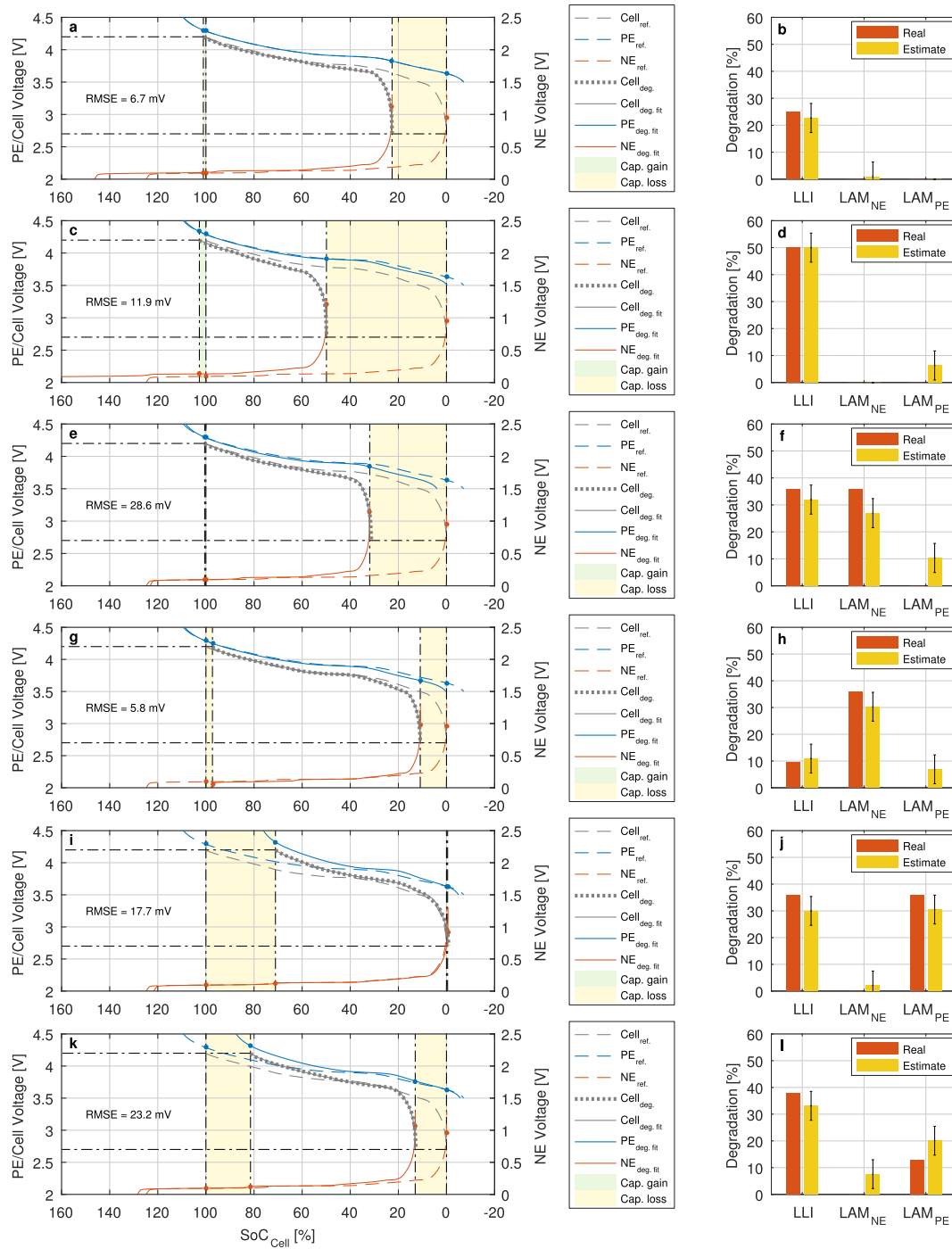
Fig. 8. Results of degradation diagnostics; fitted cell OCVs (left column) and estimated degradation mode (right column). a) and b): cell LLI25, c) and d): cell LLI50, e) and f): cell LAM$_{NE,li}$, g) and h): cell LAM$_{NE,de}$, i) and j): cell LAM$_{PE,li}$, k) and l): cell LLI + LAM$_{PE,li}$.

was also identified exceeds the margin of error by only ∼ 1% and is therefore considered negligible.

4.3.5. 36% LAM$_{PE,li}$

Fig. 8 i) and j) display the fitted OCV and estimated degradation mode of cell LAM$_{PE,li}$ (36% of LAM$_{PE,li}$). Fig. 8 i) illustrates the effect of lost lithiated PE material on the cell's capacity, which is significantly reduced at the EoC. The correct amounts of LAM$_{PE}$ and LLI contained in the lost electrode material were estimated using the diagnostic algorithm.

4.3.6. 25% LLI + 13% LAM$_{PE,li}$

Fig. 8 k) and l) show the fitted OCV and estimated degradation mode of cell LLI + LAM$_{PE,li}$ (25% of LLI and 13% of LAM$_{PE,li}$). In this case, two degradation modes were combined. The total amount of LLI (38%) includes the pure LLI (25%) and the lithium lost inside the active PE material (13%). The yellow area at the EoC in Fig. 8 k) represents the capacity loss due to LAM$_{PE,li}$ and the yellow area at the EoD the capacity loss due to pure LLI. As shown in Fig. 8 l), the total amount of LLI was accurately estimated and the LAM$_{PE}$ was slightly overestimated, exceeding the margin of error by 1.6%. A

small amount of LAM$_{NE}$ was detected, exceeding the margin of error by $\sim 1\%$. This could be due to the same effect as described for cell LAM$_{NE,li}$. Overall, the predominant degradation modes were successfully identified, even in the presence of two independent degradation modes.

5. Conclusions

This work has built on the theory of degradation modes in Li-ion cells as a manifestation of a host of different physical and chemical mechanisms. The general theory behind the degradation modes LLI, LAM$_{PE}$ and LAM$_{NE}$ has been expanded to account for the effects of imposed upper and lower cell voltage limits on the different degradation modes. This expanded theory was used to create a diagnostic algorithm to identify and quantify LLI, LAM$_{PE}$ and LAM$_{NE}$ using only pseudo-OCV measurements of full cells. The diagnostic algorithm was validated using test cells with known amounts of LLI, LAM$_{PE}$ and LAM$_{NE}$. The results led to three key findings:

- Experimental proof of the effects of LLI, LAM$_{PE}$ and LAM$_{NE}$ on the cell's OCV.
- A diagnostic algorithm has been demonstrated to successfully identify and quantify LLI, LAM$_{PE}$ and LAM$_{NE}$.
- The diagnostic algorithm can identify the onset of potentially dangerous processes such as excessively high voltages on the PE and lithium plating on the NE.

Experimental evidence has been presented to prove, for the first time, that the OCV of Li-ion cells can be used to provide accurate estimates of LLI, LAM$_{PE}$ and LAM$_{NE}$. The diagnostic algorithm was evaluated for six different scenarios of degradation modes. Once the OCV model has been parameterized, the diagnostic algorithm requires only pseudo-OCV measurements. Since the algorithm uses the pseudo-OCV measurements as a direct input, rather than the derivative of voltage or capacity, it is less sensitive to noise compared to other techniques proposed in the literature. These attributes, combined with the low computational complexity of the diagnostic algorithm, make it ideal for BMS applications in order to keep track of the cells' SoH and to maintain safe operation.

Theoretically, the presented diagnostic technique can be applied to any Li-ion cell chemistry. This possibility will be investigated in future work. Further work also includes the identification and quantification of degradation modes in commercial Li-ion cells aged in a variety of use cases and throughout their service life. This should enable projections of the end-of-life for commercial Li-ion cells.

Acknowledgements

References

[1] S.S. Choi, H.S. Lim, Factors that affect cycle-life and possible degradation mechanisms of a Li-ion cell based on LiCoO2, J. Power Sources 111 (1) (2002) 130–136, http://dx.doi.org/10.1016/S0378-7753(02)00305-1.

[2] M. Broussely, P. Biensan, F. Bonhomme, P. Blanchard, S. Herreyre, K. Nechev, R. Staniewicz, Main aging mechanisms in Li ion batteries, J. Power Sources 146 (1–2) (2005) 90–96, http://dx.doi.org/10.1016/j.jpowsour.2005.03.172.

[3] K. Jalkanen, J. Karppinen, L. Skogström, T. Laurila, M. Nisula, K. Vuorilehto, Cycle aging of commercial NMC/graphite pouch cells at different temperatures, Appl. Energy 154 (2015) 160–172, http://dx.doi.org/10.1016/j.apenergy.2015.04.110. URL, http://linkinghub.elsevier.com/retrieve/pii/S0306261915005735.

[4] I. Bloom, B. Cole, J. Sohn, S. Jones, E. Polzin, V. Battaglia, G. Henriksen, C. Motloch, R. Richardson, T. Unkelhaeuser, D. Ingersoll, H. Case, An accelerated calendar and cycle life study of Li-ion cells, J. Power Sources 101 (2)

(2001) 238–247, http://dx.doi.org/10.1016/S0378-7753(01)00783-2. URL, http://linkinghub.elsevier.com/retrieve/pii/S0378775301007832.

[5] J. Vetter, P. Novák, M.R. Wagner, C. Veit, K.-C. Möller, J.O. Besenhard, M. Winter, M. Wohlfahrt-Mehrens, C. Vogler, A. Hammouche, Ageing mechanisms in lithium-ion batteries, J. Power Sources 147 (1–2) (2005) 269–281, http://dx.doi.org/10.1016/j.jpowsour.2005.01.006.

[6] D. Aurbach, B. Markovsky, I. Weissman, E. Levi, Y. Ein-Eli, On the correlation between surface chemistry and performance of graphite negative electrodes for Li ion batteries, Electrochim. Acta 45 (1–2) (1999) 67–86, http://dx.doi.org/10.1016/S0013-4686(99)00194-2. URL, http://linkinghub.elsevier.com/retrieve/pii/S0013468699001942.

[7] V. Agubra, J. Fergus, Lithium ion battery anode aging mechanisms, Materials 6 (4) (2013) 1310–1325, http://dx.doi.org/10.3390/ma6041310.

[8] S.-K. Jung, H. Gwon, J. Hong, K.-Y. Park, D.-H. Seo, H. Kim, J. Hyun, W. Yang, K. Kang, Understanding the degradation mechanisms of LiNi0.5Co0.2Mn0.3O2 cathode material in lithium ion batteries, Adv. Energy Mater. (2013), http://dx.doi.org/10.1002/aenm.201300787 n/a–n/a.

[9] P. Novák, F. Joho, M. Lanz, B. Rykart, J.-C. Panitz, D. Alliata, R. Kötz, O. Haas, The complex electrochemistry of graphite electrodes in lithium-ion batteries, J. Power Sources 97–98 (2001) 39–46, http://dx.doi.org/10.1016/S0378-7753(01)00586-9.

[10] P. Verma, P. Maire, P. Novák, A review of the features and analyses of the solid electrolyte interphase in Li-ion batteries, Electrochim. Acta 55 (22) (2010) 6332–6341, http://dx.doi.org/10.1016/j.electacta.2010.05.072.

[11] M.B. Pinson, M.Z. Bazant, Theory of SEI formation in rechargeable batteries: capacity fade, accelerated aging and lifetime prediction, J. Electrochem. Soc. 160 (2) (2012) A243–A250, http://dx.doi.org/10.1149/2.044302jes.

[12] E. Prada, D. Di Domenico, Y. Creff, J. Bernard, V. Sauvant-Moynot, F. Huet, A simplified electrochemical and thermal aging model of LiFePO4-graphite Li-ion batteries: power and capacity fade simulations, J. Electrochem. Soc. 160 (4) (2013) A616–A628, http://dx.doi.org/10.1149/2.053304jes.

[13] J. Christensen, J. Newman, Stress Generation and Fracture in Lithium Insertion Materials, 2006, pp. 293–319, http://dx.doi.org/10.1007/s10008-006-0095-1.

[14] R. Deshpande, M. Verbrugge, Y.-T. Cheng, J. Wang, P. Liu, Battery cycle life prediction with coupled chemical degradation and fatigue mechanics, J. Electrochem. Soc. 159 (10) (2012) A1730–A1738, http://dx.doi.org/10.1149/2.049210jes.

[15] M. Safari, M. Morcrette, A. Teyssot, C. Delacourt, Multimodal physics-based aging model for life prediction of Li-Ion batteries, J. Electrochem. Soc. 156 (3) (2009) A145, http://dx.doi.org/10.1149/1.3043429.

[16] S.J. Harris, P. Lu, Effects of inhomogeneities - nanoscale to mesoscale - on the durability of Li-Ion batteries, J. Phys. Chem. C 117 (2013) 6481–6492.

[17] T.C. Bach, S.F. Schuster, E. Fleder, J. Müller, M.J. Brand, H. Lorrmann, A. Jossen, G. Sextl, Nonlinear aging of cylindrical lithium-ion cells linked to heterogeneous compression, J. Energy Storage 5 (2016) 212–223, http://dx.doi.org/10.1016/j.est.2016.01.003.

[18] V. Pop, H.J. Bergveld, P.P.L. Regtien, J.H.G. Op het Veld, D. Danilov, P.H.L. Notten, Battery aging and its Influence on the electromotive force, J. Electrochem. Soc. 154 (8) (2007) A744, http://dx.doi.org/10.1149/1.2742296.

[19] M. Dubarry, C. Truchot, B.Y. Liaw, Synthesize battery degradation modes via a diagnostic and prognostic model, J. Power Sources 219 (2012) 204–216, http://dx.doi.org/10.1016/j.jpowsour.2012.07.016. URL, http://linkinghub.elsevier.com/retrieve/pii/S0378775312011330.

[20] K. Striebel, J. Shim, A. Sierra, H. Yang, X. Song, R. Kostecki, K. McCarthy, The development of low cost lifepo 4-based high power lithium-ion batteries, J. Power Sources 146 (1) (2005) 33–38.

[21] E. Sarasketa-Zabala, F. Aguesse, I. Villarreal, L. Rodriguez-Martinez, C. López, P. Kubiak, Understanding lithium inventory loss and sudden performance fade in cylindrical cells during cycling with deep-discharge steps, J. Phys. Chem. C 119 (2) (2014) 896–906.

[22] G.L. Plett, Extended Kalman filtering for battery management systems of LiPB-based HEV battery packs. Part 3. State and parameter estimation, J. Power Sources 134 (2) (2004) 277–292, http://dx.doi.org/10.1016/j.jpowsour.2004.02.033. URL, http://linkinghub.elsevier.com/retrieve/pii/S0378775304003611.

[23] J. Remmlinger, M. Buchholz, M. Meiler, P. Bernreuter, K. Dietmayer, State-of-health monitoring of lithium-ion batteries in electric vehicles by on-board internal resistance estimation, J. Power Sources 196 (12) (2011) 5357–5363, http://dx.doi.org/10.1016/j.jpowsour.2010.08.035.

[24] M.A. Roscher, O.S. Bohlen, D.U. Sauer, Reliable state estimation of multicell Lithium-ion battery systems, IEEE Trans. Energy Convers. 26 (3) (2011) 737–743, http://dx.doi.org/10.1109/TEC.2011.2155657.

[25] H.M. Dahn, A.J. Smith, J.C. Burns, D.A. Stevens, J.R. Dahn, User-friendly differential voltage analysis freeware for the analysis of degradation mechanisms in Li-Ion batteries, J. Electrochem. Soc. 159 (9) (2012) A1405–A1409, http://dx.doi.org/10.1149/2.013209jes.

[26] A. Marongiu, N. Nlandi, Y. Rong, D.U. Sauer, On-board capacity estimation of lithium iron phosphate batteries by means of half-cell curves, J. Power Sources 324 (2016) 158–169, http://dx.doi.org/10.1016/j.jpowsour.2016.05.041. URL, http://www.sciencedirect.com/science/article/pii/S0378775316305778.

[27] M. Dubarry, V. Svoboda, R. Hwu, B. Yann Liaw, Incremental capacity analysis and close-to-equilibrium OCV measurements to quantify capacity fade in commercial rechargeable lithium batteries, Electrochem. Solid-State Lett. 9 (10) (2006) A454–A457, http://dx.doi.org/10.1149/1.2221767. URL, http://esl.ecsdl.org/content/9/10/A454.abstract.

[28] I. Bloom, A.N. Jansen, D.P. Abraham, J. Knuth, S.A. Jones, V.S. Battaglia, G.L. Henriksen, Differential voltage analyses of high-power, lithium-ion cells 1. Technique and application, J. Power Sources 139 (1—2) (2005) 295—303, http://dx.doi.org/10.1016/j.jpowsour.2004.07.021.

[29] X. Han, M. Ouyang, L. Lu, J. Li, Y. Zheng, Z. Li, A comparative study of commercial lithium ion battery cycle life in electrical vehicle: aging mechanism identification, J. Power Sources 251 (2014) 38—54, http://dx.doi.org/10.1016/j.jpowsour.2013.11.029. URL, http://linkinghub.elsevier.com/retrieve/pii/S0378775313018569.

[30] T. Ohsaki, T. Kishi, T. Kuboki, N. Takami, N. Shimura, Y. Sato, M. Sekino, A. Satoh, Overcharge reaction of lithium-ion batteries, J. Power Sources 146 (1-2) (2005) 97—100, http://dx.doi.org/10.1016/j.jpowsour.2005.03.105.

[31] F. Orsini, A. Du Pasquier, B. Beaudoin, J. Tarascon, M. Trentin, N. Langenhuizen, E. De Beer, P. Notten, In situ Scanning Electron Microscopy (SEM) observation of interfaces within plastic lithium batteries, J. Power Sources 76 (1998) 19—29, http://dx.doi.org/10.1016/S0378-7753(98)00128-1.

[32] S. Santhanagopalan, P. Ramadass, J.Z. Zhang, Analysis of internal short-circuit in a lithium ion cell, J. Power Sources 194 (1) (2009) 550—557, http://dx.doi.org/10.1016/j.jpowsour.2009.05.002. URL, http://linkinghub.elsevier.com/retrieve/pii/S037877530900843X.

[33] C.R. Birkl, E. McTurk, M.R. Roberts, P.G. Bruce, D.A. Howey, A parametric open circuit voltage model for lithium ion batteries, J. Electrochem. Soc. 162 (12) (2015) A2271—A2280, http://dx.doi.org/10.1149/2.0331512jes. URL, http://jes.ecsdl.org/content/162/12/A2271.abstract.

[34] M. Petzl, M.A. Danzer, Nondestructive detection, characterization, and quantification of lithium plating in commercial lithium-ion batteries, J. Power Sources 254 (2014) 80—87, http://dx.doi.org/10.1016/j.jpowsour.2013.12.060.